Theory of carrier dynamics and time resolved reflectivity in $In_xMn_{1-x}As/GaSb$ heterostructures

G. D. Sanders and C. J. Stanton
Department of Physics, University of Florida, Box 118440, Gainesville, Florida 32611-8440, USA

J. Wang and J. Kono
Department of Electrical and Computer Engineering, Rice Quantum Institute, and Center for Nanoscale Science and Technology, Rice University, Houston, Texas 77005, USA

A. Oiwa and H. Munekata
Imaging Science and Engineering Laboratory, Tokyo Institute of Technology, 4259 Nagatsuta, Yokohama 226-8503, Japan
(Received 6 September 2005; published 2 December 2005)

We present detailed theoretical calculations of two color, time-resolved pump-probe differential reflectivity measurements. The experiments modeled were performed on $In_xMn_{1-x}As/GaSb$ heterostructures and have shown pronounced oscillations in the differential reflectivity as well as a time-dependent background signal. Previously, we showed that the oscillations resulted from a generation of coherent acoustic phonon wave packets in the epilayer and were not associated with the ferromagnetism. Now we take into account not only the oscillations, but also the background signal which arises from photoexcited carrier effects. The two color pump-probe reflectivity experiments are modeled using a Boltzmann equation formalism. We include photogeneration of hot carriers in the $In_xMn_{1-x}As$ quantum well by a pump laser and their subsequent cooling and relaxation by emission of confined LO phonons. Recombination of electron-hole pairs via the Schockley-Read carrier trapping mechanism is included in a simple relaxation time approximation. The time-resolved differential reflectivity in the heterostructure is obtained by solving Maxwell's equations and by comparing the experiments. Phase space filling, carrier capture and trapping, band-gap renormalization, and induced absorption are all shown to influence the spectra.

DOI: 10.1103/PhysRevB.72.245302 PACS number(s): 75.50.Pp, 85.75.−d

I. INTRODUCTION

Dilute magnetic semiconductors (DMS) made of (III,Mn)V materials have recently garnered much attention owing to the discovery of carrier mediated ferromagnetism. This offers the intriguing possibility of their use in the development of semiconductor spintronic devices capable of simultaneously performing information processing, data storage, and communication functions.[1–3]

Time-independent optical studies such as cyclotron resonance of III-V DMS materials have provided important information on effective masses and electronic structure,[4] exchange parameters,[5,6] carrier densities,[7] and whether carriers are localized or itinerant.[8]

Time-dependent optical studies are even more useful and can provide information that static magnetization or electrical transport measurements cannot. In this paper, we report on our theoretical calculations and modeling of femtosecond, time-resolved differential reflectivity spectroscopy of $In_xMn_{1-x}As/GaSb$ heterostructures. Femtosecond transient reflectivity spectroscopy has proven useful in studying carrier dynamics in semiconductors as well as the generation and propagation of coherent phonons in a number of materials. In particular, coherent optical phonons have been observed in bulk semiconductors[9,10] and coherent acoustic phonons have been detected in $In_xGa_{1-x}N/GaN$-based semiconductor heterostructures.[11–14]

The experiments we model are two-color pump-probe differential reflectivity measurements. In these experiments, there are several changes to the reflectivity on different time scales. On the fast time scale, there are changes to the reflectivity associated with ultrashort carrier lifetimes (~2 ps) and multilevel dynamics.

In addition, pronounced oscillations are observed on a longer time scale (~23 ps period).[15] Similar behavior was seen in $In_xGa_{1-x}MnAs$ systems.[16] Originally these oscillations were thought to be associated with the ferromagnetism in the $In_xMn_{1-x}As$ layer since oscillations were not observed in samples without Mn. However, we showed in a previous work[15] that the oscillations instead resulted from selective photoexcitation in the $In_xMn_{1-x}As$ layer which triggered a coherent phonon wave packet that propagated into the GaSb layer.

In this paper, we expand upon our previous work and show that the large strength of the coherent phonon oscillations results from a fortuitous strong dependence on the strain of the GaSb dielectric function near the probe energy. In addition, we also model the fast time dependent background signal which arises from the photoexcited carriers. There are three main contributions to this transient background signal: (1) the enhanced Drude absorption resulting from the photoinduced increase in free carriers, (2) the relaxation dynamics associated with the decay of the highly nonequilibrium photoexcited carrier distribution, and (3) the trapping and subsequent nonradiative recombination of photoexcited carriers due to the high density of defects in the $In_xMn_{1-x}As$ layer.

We model the experiments by first calculating the detailed electronic structure in the $In_xMn_{1-x}As$ layer. We then use a Boltzmann equation formalism to account for the photoex-

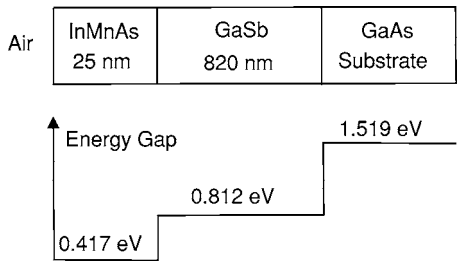

FIG. 1. Schematic diagram of the heterostructure consisting of a 25 nm $In_{0.91}Mn_{0.09}As$ quantum well and a 820 nm GaSb barrier grown on a GaAs substrate. The band gap as a function of position in each of the layers is also shown.

cited carrier dynamics. We include band-gap renormalization, carrier-phonon scattering, and carrier-trapping and/or recombination through the Shockley-Read mechanism. To determine the optical properties, we solve Maxwell's equations in the heterostructure. Details of the experiments and the calculations are given in the following sections.

II. EXPERIMENT

The main sample studied (shown schematically in Fig. 1) was an $In_xMn_{1-x}As/GaSb$ heterostructure, consisting of a 25 nm thick magnetic layer with Mn concentration 0.09, grown on a 820 nm thick GaSb buffer layer on a semi-insulating GaAs (001) substrate. Its room temperature hole density and mobility were 1.1×10^{19} cm^{-3} and 323 cm^2/V s, respectively, estimated from Hall measurements. Detailed growth conditions and sample information can be found in Ref. 17.

We performed two-color time-resolved differential reflectivity spectroscopy using femtosecond midinfrared pump pulses (2 μm, $\sim$140 fs) and a white light continuum probe (0.5–1.4 μm, $\sim$340 fs). Experimental details are described in Ref. 18.

The source of intense mid infrared pulses was an optical parametric amplifier (OPA) pumped by a Ti:sapphire-based regenerative amplifier (Model CPA-2010, Clark-MXR, Inc., 7300 West Huron River Drive, Dexter, MI 48130). At the pump wavelength (2 μm), the photon energy (0.62 eV) was just above the band gap of $In_xMn_{1-x}As$, so the created carriers had only a small amount of extra kinetic energy ($\sim$0.2 eV at 15 K), minimizing contributions from intervalley scattering and intraband relaxation. A white light continuum generated by focusing a small fraction of the CPA pulses into a sapphire crystal was used as a probe, which allowed us to probe a wide energy range far above the quasi-Fermi-level of the optically excited carriers.

III. THEORY

A. Bulk $In_xMn_{1-x}As$ band structure

In our pump-probe reflectivity experiments carriers are created in the $In_xMn_{1-x}As$ layer by pumping below the GaSb band gap. We treat the photogenerated carriers (electrons and holes) in an eight-band $\mathbf{k}\cdot\mathbf{p}$ effective mass model which includes conduction electrons, heavy holes, light holes, and split-off holes. Following Pidgeon and Brown[19] we find it convenient to separate the eight Bloch basis states into upper and lower sets which decouple at the zone center. The Bloch basis states for the upper set are

$$|1\rangle = \left|\tfrac{1}{2}, +\tfrac{1}{2}\right\rangle = |S\uparrow\rangle, \tag{1a}$$

$$|2\rangle = \left|\tfrac{3}{2}, +\tfrac{3}{2}\right\rangle = \frac{1}{\sqrt{2}}|(X+iY)\uparrow\rangle, \tag{1b}$$

$$|3\rangle = \left|\tfrac{3}{2}, -\tfrac{1}{2}\right\rangle = \frac{1}{\sqrt{6}}|(X-iY)\uparrow + 2Z\downarrow\rangle, \tag{1c}$$

$$|4\rangle = \left|\tfrac{1}{2}, -\tfrac{1}{2}\right\rangle = \frac{i}{\sqrt{3}}|-(X-iY)\uparrow + Z\downarrow\rangle, \tag{1d}$$

which correspond to electron spin up, heavy hole spin up, light hole spin down, and split off hole spin down. Likewise, the Bloch basis states for the lower set are

$$|5\rangle = \left|\tfrac{1}{2}, -\tfrac{1}{2}\right\rangle = |S\downarrow\rangle, \tag{2a}$$

$$|6\rangle = \left|\tfrac{3}{2}, -\tfrac{3}{2}\right\rangle = \frac{i}{\sqrt{2}}|(X-iY)\downarrow\rangle, \tag{2b}$$

$$|7\rangle = \left|\tfrac{3}{2}, +\tfrac{1}{2}\right\rangle = \frac{i}{\sqrt{6}}|(X+iY)\downarrow - 2Z\uparrow\rangle, \tag{2c}$$

$$|8\rangle = \left|\tfrac{1}{2}, +\tfrac{1}{2}\right\rangle = \frac{1}{\sqrt{3}}|(X+iY)\downarrow + Z\uparrow\rangle, \tag{2d}$$

corresponding to electron spin down, heavy hole spin down, light hole spin up, and split off hole spin up.

The effective-mass Hamiltonian in bulk zinc blende materials in the axial approximation is given explicitly by[20]

$$H_0 = \begin{bmatrix} H_{uu} & H_{ul} \\ H_{lu} & H_{ll} \end{bmatrix} \tag{3}$$

where H_{uu}, H_{ul}, H_{lu}, and H_{ll} are 4×4 submatrices. The effective-mass Hamiltonian matrix elements between the upper set basis states in Eq. (1) are

$$H_{uu} = \begin{bmatrix} E_g + A & i\frac{\sqrt{2}}{2}Vk_+ & i\frac{\sqrt{6}}{6}Vk_- & \frac{\sqrt{3}}{3}Vk_- \\ -i\frac{\sqrt{2}}{2}Vk_- & -P-Q & -M & i\sqrt{2}M \\ -i\frac{\sqrt{6}}{6}Vk_+ & -M^\dagger & -P+Q & i\sqrt{2}Q \\ \frac{\sqrt{3}}{3}Vk_+ & -i\sqrt{2}M^\dagger & -i\sqrt{2}Q & -\Delta-P \end{bmatrix}, \tag{4a}$$

while the Hamiltonian matrix elements between the lower set basis states in Eq. (2) are given by

$$H_{ll}=\begin{bmatrix} E_g+A & -\frac{\sqrt{2}}{2}Vk_- & -\frac{\sqrt{6}}{6}Vk_+ & i\frac{\sqrt{3}}{3}Vk_+ \\ -\frac{\sqrt{2}}{2}Vk_+ & -P-Q & -M^\dagger & i\sqrt{2}M^\dagger \\ -\frac{\sqrt{6}}{6}Vk_- & -M & -P+Q & i\sqrt{2}Q \\ -i\frac{\sqrt{3}}{3}Vk_- & -i\sqrt{2}M & -i\sqrt{2}Q & -\Delta-P \end{bmatrix}. \tag{4b}$$

The submatrices coupling upper and lower set basis states are

$$H_{ul}=\begin{bmatrix} 0 & 0 & \frac{\sqrt{6}}{3}Vk_z & i\frac{\sqrt{3}}{3}Vk_z \\ 0 & 0 & -L & -i\frac{\sqrt{2}}{2}L \\ -i\frac{\sqrt{6}}{3}Vk_z & L & 0 & i\frac{\sqrt{6}}{2}L^\dagger \\ -\frac{\sqrt{3}}{3}Vk_z & -i\frac{\sqrt{2}}{2}L & i\frac{\sqrt{6}}{2}L^\dagger & 0 \end{bmatrix}, \tag{4c}$$

and

$$H_{lu}=\begin{bmatrix} 0 & 0 & i\frac{\sqrt{6}}{3}Vk_z & -\frac{\sqrt{3}}{3}Vk_z \\ 0 & 0 & L^\dagger & i\frac{\sqrt{2}}{2}L^\dagger \\ \frac{\sqrt{6}}{3}Vk_z & -L^\dagger & 0 & -i\frac{\sqrt{6}}{2}L \\ -i\frac{\sqrt{3}}{3}Vk_z & i\frac{\sqrt{2}}{2}L^\dagger & -i\frac{\sqrt{6}}{2}L & 0 \end{bmatrix}. \tag{4d}$$

In Eqs. (4) E_g is the bulk band gap, Δ is the spin orbit splitting, and $k_\pm=k_x\pm i\,k_y$. Following Jain *et al.*,[21] band-gap renormalization in InAs shrinks the InAs band gap by an amount

$$\Delta E_g = AN^{1/3}+BN^{1/4}+C\sqrt{N}, \tag{5}$$

where N is the electron or hole carrier concentration and A, B, and C are material parameters which are found to be different for electrons and holes. The temperature dependence of the band gap is taken into account using the empirical Varshni formula.[22] The temperature and carrier dependent band gap is given by

$$E_g(T,N)=E_g-\frac{\alpha_v T^2}{T+\beta_v}-\Delta E_g, \tag{6}$$

where α_v and β_v are Varshni parameters that are tabulated in Ref. 23 for a variety of semiconductors. The Kane momentum matrix element $V=(-i\hbar/m_0)\langle S|p_x|X\rangle$ is related to the optical matrix element E_p by[23]

$$V=\sqrt{\frac{\hbar^2}{m_0}\frac{E_p}{2}}. \tag{7}$$

The operators A, P, Q, L, and M are

$$A=\frac{\hbar^2}{m_0}\frac{\gamma_4}{2}(k_\parallel^2+k_z^2), \tag{8a}$$

$$P=\frac{\hbar^2}{m_0}\frac{\gamma_1}{2}(k_\parallel^2+k_z^2), \tag{8b}$$

$$Q=\frac{\hbar^2}{m_0}\frac{\bar{\gamma}}{2}(k_\parallel^2-2k_z^2), \tag{8c}$$

$$L=-i\frac{\hbar^2}{m_0}\sqrt{3}\bar{\gamma}(k_x-ik_y)k_z, \tag{8d}$$

and

$$M=\frac{\hbar^2}{m_0}\frac{\sqrt{3}}{2}\bar{\gamma}(k_x-ik_y)^2, \tag{8e}$$

where $k_\parallel^2=k_x^2+k_y^2$. In the axial approximation,[24] we have $\bar{\gamma}=(2\gamma_2+3\gamma_3)/5$ so that the energy bands depend only on the magnitude of $\mathbf{k}_\parallel$. Note that at $k_z=0$, the effective mass Hamiltonain in Eq. (3) is block diagonal since $L=0$ at $k_z=0$.

In Eq. (8), the parameters γ_1 and $\bar{\gamma}$ are not the usual Luttinger parameters since this is an eight-band model, but instead are related to the usual Luttinger parameters γ_1^L and $\bar{\gamma}^L$ by the relations[25]

$$\gamma_1=\gamma_1^L-\frac{E_p}{3E_g} \tag{9}$$

and

$$\bar{\gamma}=\bar{\gamma}^L-\frac{E_p}{6E_g}. \tag{10}$$

This takes into account the additional coupling of the valence bands to the conduction band not present in the six-band Luttinger model for the valence bands.

The parameter γ_4 is related to the conduction-band effective mass m_e^* through the relation[20]

$$\gamma_4=\frac{1}{m_e^*}-\frac{E_p}{3}\left(\frac{2}{E_g}+\frac{1}{E_g+\Delta}\right). \tag{11}$$

The exchange interaction between the Mn^{2+} d electrons and the conduction s and valence p electrons is treated in the virtual crystal and molecular field approximation. The resulting Mn exchange Hamiltonian is[26]

$$H_{Mn}=xN_0\langle S_z\rangle\begin{bmatrix} D_a & 0 \\ 0 & -D_a \end{bmatrix}, \tag{12}$$

where x is the Mn concentration, N_0 is the number of cation sites in the sample, and $\langle S_z\rangle$ is the average spin on a Mn site. The 4×4 submatrix D_a is

$$D_a = \begin{bmatrix} \frac{1}{2}\alpha & 0 & 0 & 0 \\ 0 & \frac{1}{2}\beta & 0 & 0 \\ 0 & 0 & -\frac{1}{6}\beta & -i\frac{\sqrt{2}}{3}\beta \\ 0 & 0 & i\frac{\sqrt{2}}{3}\beta & \frac{1}{2}\beta \end{bmatrix}, \tag{13}$$

where α and β are the *s-d* and *p-d* exchange integrals.

The average Mn spin $\langle S_z \rangle$ in the ferromagnetic $In_{1-x}Mn_xAs$ quantum well is computed in the mean field approximation, i.e.,

$$\langle S_z \rangle = -SB_S\left(-\frac{JS\langle S_z \rangle}{kT}\right), \tag{14}$$

where $B_S(x)$ is the Brillouin function, $S=\frac{5}{2}$ for the $3d^5$ electrons of the the Mn^{2+} ion,[27] $J=3k_BT_c/S(S+1)$ is the ferromagnetic coupling, and T_c is the experimentally measured Curie temperature.

The effective mass Hamiltonian for $In_{1-x}Mn_xAs$ is

$$H = H_0 + H_{Mn}. \tag{15}$$

It is assumed in our calculations that the compensation arises from As antisites and hence the effective Mn fraction x in Eq. (12) is taken to be equal to the actual Mn fraction in the sample. We note that this is supported by experimental evidence showing that InAs grown at low temperature (200 °C) is a homogeneous alloy and that the magnetization varies linearly with Mn content, x.[28–31]

B. Confined states in the $In_xMn_{1-x}As$ quantum well

In quantum-confined systems such as the $In_xMn_{1-x}As$ quantum well shown in Fig. 1, we must modify the bulk Hamiltonian in Eq. (15). The quantum well breaks translational symmetry along the z direction but not in the x-y plane. Since the pump pulse is below the GaSb band gap, all photogenerated electrons and holes are strongly confined to the well and we assume the confinement potentials are infinite. The wave functions in the envelope function approximation are

$$\psi_{n,\mathbf{k}_\parallel}(r) = \frac{e^{i\mathbf{k}_\parallel\cdot\rho}}{\sqrt{A}}\sum_{\nu=1}^{8} F_{n,\nu,\mathbf{k}_\parallel}(z)|\nu\rangle, \tag{16}$$

where A is the cross sectional area of the sample, n is the subband index, $\mathbf{k}_\parallel=(k\cos\theta, k\sin\theta, 0)$ is the two-dimensional wave vector and $|\nu\rangle=|1\rangle,\ldots,|8\rangle$ are the Bloch basis states defined in Eqs. (1) and (2). The complex valued envelope functions $F_{n,\nu,\mathbf{k}_\parallel}(z)$ are slowly varying in comparison with the Bloch basis states.

The envelope functions satisfy a set of effective-mass Schrödinger equations which, in the axial approximation, are

$$\sum_{\nu'=1}^{8} H_{\nu,\nu'}(\mathbf{k}_\parallel)F_{n,\nu',\mathbf{k}_\parallel}(z) = E_n(k)F_{n,\nu,\mathbf{k}_\parallel}(z) \tag{17}$$

subject to the boundary condition that the envelope functions vanish at the walls of the quantum well. The operators $H_{\nu,\nu'}(\mathbf{k}_\parallel)$ depend on the wave vector in the x-y plane and can be obtained from the matrix elements in Eq. (15) by making the operator replacement $k_z \rightarrow -i\partial/\partial z$ in all the matrix elements of Eq. (3).

In practice, we solve for the envelope functions for a given value of $\mathbf{k}_\parallel$ on an evenly spaced mesh of points, z_i, $i=1\ldots N$, in the quantum well. Approximating the derivative, $\partial/\partial z$ by a finite difference formula, the Schrödinger equation (17) with the rigid wall boundary conditions becomes a matrix eigenvalue problem which can be solved for the eigenvalues $E_n(\mathbf{k}_\parallel)$ and the complex envelope functions $F_{n,\nu,\mathbf{k}_\parallel}(z_i)$ evaluated at the mesh points, z_i.

C. Boltzmann transport equations

In the two-color time-resolved differential reflectivity experiments the pump laser is used to promote electrons from the valence to the conduction subbands of the quantum well. The photoexcited carriers then relax through scattering, changing the optical properties of the heterostructure in the process. These processes are often simulated using Boltzmann transport equations.

In this paper, we formulate and solve the Boltzmann transport equations using a numerical method similar to the one described in Ref. 32. For each subband state with energy, $E_n(k)$, we have a time-dependent distribution function $f_n(\mathbf{k}_\parallel,t)$ which gives the probability, as a function of time, of finding an electron in subband n with wave vector $\mathbf{k}_\parallel$. The Boltzmann equation including photogeneration of hot electron-hole pairs by the pump, the subsequent cooling of these carriers by emission of confined LO phonons, and the recombination of electron-hole pairs by means of carrier trapping is

$$\frac{\partial f_n(\mathbf{k}_\parallel)}{\partial t} = \sum_{n',k'_\parallel}\{f_{n'}(\mathbf{k}'_\parallel)W^{n',n}_{\mathbf{k}'_\parallel,\mathbf{k}_\parallel}[1-f_n(\mathbf{k}_\parallel)] - f_n(\mathbf{k}_\parallel)W^{n,n'}_{\mathbf{k}_\parallel,\mathbf{k}'_\parallel}[1-f_{n'}(\mathbf{k}'_\parallel)]\} + \left[\frac{\partial f_n(\mathbf{k}_\parallel)}{\partial t}\right]. \tag{18}$$

The scattering rate due to scattering by confined LO phonons in the quantum well, $W^{n,n'}_{\mathbf{k}_\parallel,\mathbf{k}'_\parallel}$, is the rate at which electrons in subband n with wave vector $\mathbf{k}_\parallel$ scatter to subband n' with wave vector $\mathbf{k}'_\parallel$. The last term on the right-hand side of Eq. (18) describes the change in the electron distribution function due to the action of the pump as well as a recombination of electron-hole pairs by means of carrier trapping. Thus

$$\left[\frac{\partial f_n(\mathbf{k}_\parallel)}{\partial t}\right] = \left[\frac{\partial f_n(\mathbf{k}_\parallel)}{\partial t}\right]_P + \left[\frac{\partial f_n(\mathbf{k}_\parallel)}{\partial t}\right]_T, \tag{19}$$

where the first term on the right hand-side is the photogeneration rate and the second term is the recombination rate due to carrier trapping.

To simplify the calculations, we use an axial approximation in which the distribution functions are replaced by their angular averages in the x-y plane of the quantum well. The axial distribution functions are

$$f_n(k,t) = \int_{-\pi}^{\pi} \frac{d\theta}{2\pi} f_n(\mathbf{k}_\parallel, t) = \int_{-\pi}^{\pi} \frac{d\theta}{2\pi} f_n(k,\theta,t). \tag{20}$$

Next, we divide k space into evenly spaced cells of width $\Delta k = k_{max}/N_k$, where N_k is the number of cells. The value of k at the midpoint of each cell is denoted k_m $(m=1\ldots N_k)$. In each k cell we define the cell averaged distribution functions

$$f_n(k_m,t) = \int_m \frac{dk\,k}{\Delta k k_m} f_n(k,t), \tag{21}$$

where the limits of integration are from $k_m - \Delta k/2$ to $k_m + \Delta k/2$.

If we assume that the distribution functions in the Boltzmann equation depend only on k and vary slowly within each k cell, we can obtain a coupled set of ordinary differential equations for the cell averaged axial distribution functions;

$$\frac{\partial f_n(k_m)}{\partial t} = \frac{A}{2\pi} \sum_{n',m'} \Delta k k'_m \{ f_{n'}(k'_m) W^{n',n}_{m',m} [1 - f_n(k_m)] - f_n(k_m) W^{n,n'}_{m,m'} [1 - f_{n'}(k'_m)] \} + \left[\frac{\partial f_n(k_m)}{\partial t}\right]. \tag{22}$$

The confined LO phonon scattering rates in the original Boltzmann equation (18) depend only on the angle Θ between $\mathbf{k}_\parallel$ and $\mathbf{k}'_\parallel$, so the cell and axially averaged scattering rates appearing in Eq. (22) are given by

$$W^{n,n'}_{m,m'} = \int_m \frac{dk\,k}{\Delta k k_m} \int_{m'} \frac{dk'\,k'}{\Delta k k_{m'}} \int_{-\pi}^{\pi} \frac{d\Theta}{2\pi} W^{n,n'}_{\mathbf{k}_\parallel, \mathbf{k}'_\parallel}. \tag{23}$$

Given initial values of the distribution function, $f_n(k_m, t \to -\infty)$, we can solve the system of coupled ordinary differential equations (22) with an adaptive Runge-Kutta routine.[33] In order for the integration to be numerically stable, we need the cell averaged scattering rates in Eq. (23) to satisfy the detailed balance condition. We ensure this by calculating the downward scattering rate and using the detailed balance condition to obtain the upward scattering rate. If $W^{n,n'}_{m,m'}$ is the cell averaged downward scattering rate between a higher lying state $E_n(k_m)$ and a lower lying state $E_{n'}(k_{m'})$, then the upward scattering rate, $W^{n',n}_{m',m}$, between these two states is

$$W^{n',n}_{m',m} = \exp\left[-\left(\frac{E_n(k_m) - E_{n'}(k_{m'})}{k_B T}\right)\right] W^{n,n'}_{m,m'}. \tag{24}$$

The electrons are initially in thermal equilibrium with the lattice and are described by a Fermi-Dirac distribution

$$f^0_n(k_m) = \frac{1}{1 + \exp\{[E_n(k_m) - E_F]/k_B T\}}. \tag{25}$$

If n and p are the initial electron and hole column densities in the quantum well, then the Fermi energy as a function of the lattice temperature and initial carrier concentrations can be easily found by solving

$$n - p = \frac{1}{2\pi} \sum_{n,m} \Delta k k_m [f^0_n(k_m) - \delta_{n,v}] \tag{26}$$

for E_F using a root finding routine.[33] In Eq. (26) the valence delta function $\delta_{n,v}$ is defined as zero if subband n is a conduction subband and one if subband n is a valence subband.

To finish specifying the transport problem, we need to supply the cell averaged axial scattering rates appearing in Eq. (22) as well as the cell averaged photogeneration and carrier trapping term.

D. Photogeneration rates

The photogeneration rate is computed using Fermi's golden rule. The pump is characterized by the fluence which is the total flux integrated over time. Assuming a narrow spectral width for the pump, centered on the pump energy $\hbar\omega$, the fluence is given by

$$F_0 = \int_{-\infty}^{\infty} U_0(t) \frac{c}{n_r}, \tag{27}$$

where $U_0(t)$ is the pump energy density and n_r is the refractive index in the $In_xMn_{1-x}As$ quantum well. For the pump energy density, we assume a Gaussian pulse shape with an intensity FWHM of τ_p so that

$$U_0(t) = \bar{U}_0 \exp\left[-4\ln(2)\left(\frac{t}{\tau_p}\right)^2\right]. \tag{28}$$

Assuming the Dirac delta function in Fermi's golden rule is the only rapidly varying quantity in a k cell, the cell averaged photogeneration rate in Eq. (19) is given by

$$\left[\frac{\partial f_n(k_m)}{\partial t}\right]_P = \frac{4\pi^2 e^2 U_0(t)}{\hbar n_r^2 (\hbar\omega)^2} \sum_{n'} |P_{n,n'}(k_m)|^2 \times [f_{n'}(k_m) - f_n(k_m)] \Delta^m_{n,n'}(\hbar\omega). \tag{29}$$

The cell averaged delta function, denoted $\Delta^m_{n,n'}(\varepsilon)$, is

$$\Delta^m_{n,n'}(\varepsilon) = \int_m \frac{dk\,k}{\Delta k k_m} \delta_\gamma[|E_{n'}(k) - E_n(k)| - \varepsilon], \tag{30}$$

where $\delta_\gamma(x)$ is a Lorentzian line shape with FWHW, γ.

The squared optical matrix element $|P_{n,n'}(k)|^2$ between subbands n and n' is the angular average

$$|P_{n,n'}(k)|^2 = \int_{-\pi}^{\pi} \frac{d\theta}{2\pi} |\boldsymbol{\epsilon} \cdot \mathbf{P}_{n,n'}(k,\theta)|^2, \tag{31}$$

where $\boldsymbol{\epsilon}$ is the unit complex polarization vector of the pump pulse. The optical matrix element between subband states at fixed $\mathbf{k}_\parallel$ is

$$\mathbf{P}_{n,n'}(\mathbf{k}_\parallel) = \frac{\hbar}{m_0} \sum_{\nu,\nu'} \langle \nu|\mathbf{p}|\nu'\rangle \int dz\, F^*_{n,\nu,\mathbf{k}_\parallel}(z) F_{n',\nu',\mathbf{k}_\parallel}(z), \tag{32}$$

where $\langle \nu|\mathbf{p}|\nu'\rangle$ is the momentum matrix element between the Bloch basis states defined in Eqs. (1) and (2). Explicit expressions for the matrix elements of $\mathbf{P}=(\hbar/m_0)\ \mathbf{p}$ between the Bloch basis states in terms of the Kane momentum matrix element, V, defined in Eq. (7) can be found in Appendix B of Ref. 5.

E. Recombination rates due to carrier trapping

Electron-hole pairs can recombine through the ultrafast trapping of electrons (by As_{Ga}, antisite defects) and holes (by Ga vacancies) by the midgap states introduced by low temperature molecular beam epitaxy growth.[15] The cell averaged carrier trapping rate in Eq. (19) is treated using a simple relaxation time model of the form

$$\left[\frac{\partial f_n(k_m)}{\partial t}\right]_T = -\left(\frac{f_n(k_m,t) - f_n^0(k_m)}{\tau(t)}\right), \tag{33}$$

where $f_n^0(k_m)$ are the initial thermal equilibrium distribution functions defined in Eq. (25) and $\tau(t)$ is the Shockley-Read recombination time for electron-hole pairs.

If we assume electron-hole pairs recombine through trapping at monovalent flaws in the midgap region, the Shockley-Read recombination time can be expressed as[34]

$$\tau(t) = \frac{(n+p)\tau_0 + n_e(t)\tau_\infty}{(n+p) + n_e(t)}, \tag{34}$$

where n and p are the initial electron and hole column densities in the quantum well and $n_e(t)$ is the column density of photogenerated electron-hole pairs. In our model, we assume for simplicity that the flaws are acceptorlike with $\tau_\infty \ll \tau_0$ so that $\tau_\infty \approx 0$.

The electron-hole pair column density is equal to the column density of *photogenerated* electrons which is given by

$$n_e(t) = \frac{1}{2\pi} {\sum_{n,m}}' \Delta k k_m [f_n(k_m,t) - f_n^0(k_m)], \tag{35}$$

where the prime on the summation sign is a reminder that the sum over subband index, n, is restricted to conduction subbands. We note in passing that the number of photogenerated electrons and holes remain equal in the Shockley-Read recombination model.

F. Confined LO phonon scattering rates

When the sample is excited by the ultrafast pump laser, hot carriers are created above the fundamental gap. The hot carriers relax back to the band edge and reach a quasithermal equilibrium through carrier cooling. The dominant cooling mechanism is absorption and emission of confined longitudinal optical (LO) phonons in the quantum well. The Frölich Hamiltonian for LO phonon scattering in a quantum well of width L is given by[32]

$$H_{LO} = \frac{C_{LO}}{\sqrt{LA}} \sum_{\mathbf{q},l} t_l(q) e^{i\mathbf{q}\cdot\rho} u_l(z) (a^\dagger_{\mathbf{q},l} + a_{-\mathbf{q},l}), \tag{36}$$

where the electron LO phonon coupling constant is given by

$$C_{LO} = \sqrt{4\pi\hbar\omega_{LO}\left(\frac{1}{\varepsilon_\infty} - \frac{1}{\varepsilon_0}\right)}. \tag{37}$$

The LO phonon energy in the Einstein model is $\hbar\omega_{LO}$ and ε_0 and ε_∞ are the static and high frequency dielectric constants in the quantum well. The operator $a^\dagger_{\mathbf{q},l}$ creates a confined LO phonon in the quantum well in the lth LO phonon mode with wave vector $\mathbf{q}$. The vibrational amplitude of the lth LO phonon mode is $u_l(z)$ and

$$\frac{1}{t_l(q)^2} = \frac{2}{L}\int_0^L dz \left[q^2 u_l(z)^2 + \left(\frac{\partial u_l(z)}{\partial z}\right)^2\right]. \tag{38}$$

The vibrational amplitude is model dependent. In the slab mode model of Fuchs and Kleiwer[35]

$$u_l(z) = \sin\left(\frac{l\pi z}{L}\right)\ l = 1,2,3,\ldots\ . \tag{39}$$

Using Fermi's golden rule, the confined LO phonon scattering rate due to emission or absorption of a single confined LO phonon is

$$\begin{aligned} W^{n,n'}_{\mathbf{k}_\parallel,\mathbf{k}'_\parallel} = {} & \frac{2\pi}{\hbar}\frac{C_{LO}^2}{LA}\sum_{l=1}^{\infty} t_l(|\mathbf{k}_\parallel - \mathbf{k}'_\parallel|)^2 |\gamma^{n,n'}_{\mathbf{k}_\parallel,\mathbf{k}'_\parallel}(l)|^2 \\ & \times [N_0 \delta(\Delta E^{n,n'}_{k,k'} + \hbar\omega_{LO}) \\ & + (N_0+1)\delta(\Delta E^{n,n'}_{k,k'} - \hbar\omega_{LO})]. \end{aligned} \tag{40}$$

The energy slitting $\Delta E^{n,n'}_{k,k'} = E_n(k) - E_{n'}(k')$ and the LO phonon occupation number N_0 is given by the Bose-Einstein distribution

$$N_0 = \frac{1}{\exp(\hbar\omega_{LO}/k_B T) - 1}. \tag{41}$$

The vibrational amplitude form factor is defined as

$$\gamma^{n,n'}_{\mathbf{k}_\parallel,\mathbf{k}'_\parallel}(l) = \sum_{\nu=1}^{8} \int dz\, F^*_{n,\nu,\mathbf{k}_\parallel}(z) u_l(z) F_{n',\nu,\mathbf{k}'_\parallel}(z). \tag{42}$$

The cell averaged scattering rates, $W^{n,n'}_{m,m'}$, used in the Bolztmann equation (22) are obtained by substituting Eq. (40) into Eq. (23) and performing the integrals.

G. Generation and propagation of coherent acoustic phonons

The ultrafast photogeneration of electrons and holes in the $In_xMn_{1-x}As$ quantum well by the pump gives rise to coherent

longitudinal acoustic (LA) phonons which propagate into the sample.[11–13,36,37] Coherent acoustic phonons, as opposed to incoherent phonons, give rise to a macroscopic lattice displacement. Since the photogenerated carrier distributions are functions of z, the transient lattice displacement $U(z,t)$ due to photogenerated carriers is independent of x and y and is parallel to z. As discussed in Refs. 36 and 11, the coherent phonon lattice displacement satisfies a loaded string equation. In the presence of a position-dependent longitudinal acoustic sound velocity $C_s(z)$ we have

$$\frac{\partial^2 U(z,t)}{\partial t^2} - \frac{\partial}{\partial z}\left(C_s(z)^2 \frac{\partial U(z,t)}{\partial z} \right) = S(z,t), \tag{43}$$

where $S(z,t)$ is the driving function. The longitudinal acoustic sound velocity is given by

$$C_s(z) = \sqrt{\frac{C_{11}(z)}{\rho_0(z)}}, \tag{44}$$

where $C_{11}(z)$ and $\rho_0(z)$ are the position dependent elastic stiffness constant and mass density.

The loaded string equation is to be solved subject to the initial conditions

$$U(z, t=-\infty) = \frac{\partial U(z, t=-\infty)}{\partial t} = 0. \tag{45}$$

We solve the loaded string equation numerically by finite differencing Eq. (43) inside a computational box whose left edge z_L is the semiconductor-air interface and whose right edge z_R lies inside the GaAs substrate (see Fig. 1). At z_R we impose absorbing boundary conditions and at z_L there are no perpendicular forces at the semiconductor-air interface. Thus we solve the initial value problem subject to the left and right boundary conditions

$$\frac{\partial U(z_L,t)}{\partial z} = 0 \tag{46a}$$

and

$$\frac{\partial U(z_R,t)}{\partial z} + \frac{1}{C_s(z_R)} \frac{\partial U(z_R,t)}{\partial t} = 0. \tag{46b}$$

Starting with the second quantized Hamiltonian for the electron-phonon interaction, a microscopic expression for the driving function was derived in Ref. 36 using the density matrix formalism (see also the erratum in Ref. 37 as well as the review article in Ref. 11). In zinc-blende materials such as InAs the electron-phonon interaction is due to deformation potential coupling. Under typical experimental conditions the microscopic expression for the driving function can be simplified to[36]

$$S(z,t) = \frac{1}{\rho_0}\left(a_c \frac{\partial \rho_e(z,t)}{\partial z} - a_v \frac{\partial \rho_h(z,t)}{\partial z} \right), \tag{47}$$

where ρ_0 is the mass density, a_c and a_v are the deformation potentials for conduction and valence bands, and $\rho_e(z,t)$ and $\rho_h(z,t)$ are the photogenerated electron and hole carrier densities. We note that this last equation was derived independently in the elastic continuum limit by Chigarev *et al.*[38] and Chern *et al.*[11] The driving function satisfies the sum rule

$$\int_{-\infty}^{\infty} dz\, S(z,t) = 0. \tag{48}$$

as shown in Refs. 36 and 11.

The photogenerated electron and hole densities can be obtained from the envelope and distribution functions described in the previous sections as

$$\rho_e(z,t) = \frac{1}{A} \sum_{n,\nu,\mathbf{k}_\parallel} [f_n(k,t) - f_n^0(k)] |F_{n,\nu,\mathbf{k}_\parallel}(z)|^2 \delta_{n,c} \tag{49a}$$

and

$$\rho_h(z,t) = \frac{1}{A} \sum_{n,\nu,\mathbf{k}_\parallel} [f_n^0(k) - f_n(k,t)] |F_{n,\nu,\mathbf{k}_\parallel}(z)|^2 \delta_{n,v}. \tag{49b}$$

The initial Fermi-Dirac distribution functions $f_n^0(k)$ are defined in Eq. (25) and $\delta_{n,c}$ and $\delta_{n,v}$ are conduction and valence delta functions that select out conduction and valence subbands, respectively.

The propagating coherent phonon displacement field $U(z,t)$ gives rise to a propagating strain tensor with components

$$\varepsilon_{zz}(z,t) = \frac{\partial U(z,t)}{\partial z} \tag{50a}$$

and

$$\varepsilon_{xx}(z,t) = \varepsilon_{yy}(z,t) = -\frac{C_{12}(z)}{C_{11}(z) + C_{12}(z)} \varepsilon_{zz}(z,t), \tag{50b}$$

where $C_{11}(z)$ and $C_{12}(z)$ are elastic stiffness constants. This propagating strain field alters the optical properties of the sample which can be detected by the probe.

H. Transient probe response

To compute the time-dependent probe transmission and reflection coefficients we need to model the dielectric function in the entire structure, i.e., the $In_xMn_{1-x}As$ well, GaSb barrier, and GaAs substrate, over the probe energy range which extends up to 2 eV. We will denote this dielectric function as

$$\varepsilon(\hbar\omega, z, t) = \varepsilon_1(\hbar\omega, z, t) + i\varepsilon_2(\hbar\omega, z, t), \tag{51}$$

where $\hbar\omega$ is the probe energy. Once the dielectric function is found, we can solve Maxwell's equations for the time-dependent probe reflection coefficient, $R(\hbar\omega, t)$, and the transmission coefficient $T(\hbar\omega, t)$ using the transfer matrix method described in detail in Ref. 39.

There are several processes which contribute to the dielectric function in the $In_xMn_{1-x}As$ quantum well. The first of these is a Drude term due to free carriers in the quantum well, which gives a real contribution to the dielectric function of

$$\varepsilon_1(\hbar\omega,z,t)_D = -\frac{[\hbar\omega_p(t)]^2}{(\hbar\omega)^2}, \tag{52}$$

where ω_p is the plasma frequency. The Drude contribution to the dielectric function in Eq. (52) is uniform in the quantum well and vanishes everywhere else. In the random phase approximation, the time-dependent plasma frequency is given by[40]

$$\omega_p^2(t) = \frac{4\pi e^2}{L}\frac{1}{A}\sum_{n,\mathbf{k}_\parallel}\frac{f_n(k,t)-\delta_{n,v}}{m_n^*(k)}, \tag{53}$$

where L is the quantum well width and A is the cross sectional area of the sample. The effective mass is

$$\frac{1}{m_n^*(k)} = \frac{1}{\hbar^2}\frac{\partial^2 E_n(k)}{\partial k^2}. \tag{54}$$

A second contribution to the dielectric function in the quantum well is due to dipole transitions between quantum confined carrier states. Using Fermi's golden rule, we obtain[39,41]

$$\varepsilon_1(\hbar\omega,z,t)_{QW} = \frac{8\pi e^2}{L}\frac{1}{A}\sum_{n,n',k_\parallel}|P_{n,n'}(k_\parallel)|^2 \times\frac{f_{n'}(k,t)-f_n(k,t)}{\Delta E_{n,n'}(k)[\Delta E_{n,n'}(k)+\hbar\omega][\Delta E_{n,n'}(k)-\hbar\omega]} \tag{55a}$$

and

$$\varepsilon_2(\hbar\omega,z,t)_{QW} = \frac{4\pi^2 e^2}{L(\hbar\omega)^2}\frac{1}{A}\sum_{n,n',k_\parallel}|P_{n,n'}(k_\parallel)|^2 \times[f_{n'}(k,t)-f_n(k,t)]\delta(\Delta E_{n,n'}(k)-\hbar\omega), \tag{55b}$$

where $\Delta E_{n,n'}(k)=E_n(k)-E_{n'}(k)$ are the transition energies, including band-gap renormalization corrections due to photogenerated carriers and $P_{n,n'}(k_\parallel)$ are the optical matrix elements. The contributions to the dielectric function in Eq. (55) are for zero linewidth. For a finite FWHM linewidth Γ, we make the replacements[39]

$$\frac{1}{\Delta E_{n,n'}(k)-\hbar\omega} \rightarrow \frac{\Delta E_{n,n'}(k)-\hbar\omega}{[\Delta E_{n,n'}(k)-\hbar\omega]^2+(\Gamma/2)^2} \tag{56}$$

and

$$\delta(x) \rightarrow \frac{1}{\pi}\frac{(\Gamma/2)}{x^2+(\Gamma/2)^2}. \tag{57}$$

There is also a background dielectric function ε_b in the quantum well due to all the higher lying electronic transitions whose real and imaginary parts we shall denote ε_{1b} and ε_{2b}. For simplicity, we treat these contributions to the dielectric function using Adachi's model dielectric function for bulk InAs with contributions from the E_0 and $E_0+\Delta_0$ critical points removed.[42,43] These correspond to contributions from the confined quantum well electronic states and are already included in Eq. (55). The background dielectric function in InAs as a function of photon energy is shown in Fig. 2 at $T=0$ K and in the absence of strain.

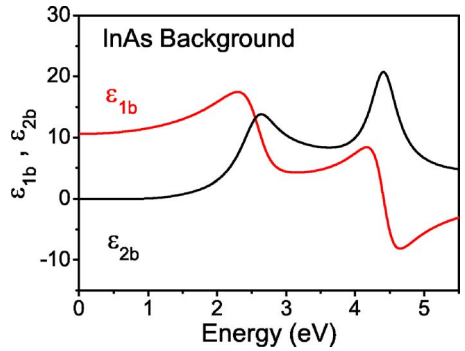

FIG. 2. (Color online) Background model dielectric function at $T=0$ K as a function of photon energy used in computing the dielectric function in the $In_xMn_{1-x}As$ quantum well.

Following Thomsen and co-workers[44,45] we assume that the dielectric function changes with strain only because of strain-induced variations in the energy gaps associated with each transition. The propagating coherent phonon strain tensor alters the optical properties of the structure through the deformation potential interaction. In our experiments, the probe photon energy can go as high as the GaSb E_1 transition region. *Ab initio* density functional calculations of the deformation potentials for the E_1 transitions in a number of semiconductors[46] have shown that the deformation potentials associated with the E_0 and E_1 features are equal to within 20%. So, to a first approximation, the effect of temperature and strain on ε_b is to introduce a rigid shift in the dielectric function such that

$$\varepsilon_b(\hbar\omega,z,t) = \varepsilon_b[\hbar\omega-\Delta E_g(T)-a_{cv}(\varepsilon_{xx}+\varepsilon_{yy}+\varepsilon_{zz})]. \tag{58}$$

Here, $a_{cv}=a_c-a_v$ is the interband deformation potential, ε_{xx}, ε_{yy}, and ε_{zz} are the coherent phonon strain tensor components defined in Eq. (50), and $\Delta E_g(T)=E_g(T)-E_g$ is the band-gap shift due to temperature variations with $E_g(T)$ being the temperature-dependent band-gap defined by the Varshni expression in Eq. (6).

The total dielectric function in the quantum well is obtained by adding the Drude, quantum well, and background contributions in Eqs. (52), (55), and (58), i.e.,

$$\varepsilon(\hbar\omega,z,t) = \varepsilon(\hbar\omega,z,t)_D + \varepsilon(\hbar\omega,z,t)_{QW} + \varepsilon_b(\hbar\omega,z,t). \tag{59}$$

We use Adachi-type model dielectric functions for the GaSb barrier[47,48] and the GaAs substrate.[49] Figure 3 shows the real and imaginary parts of the model dielectric function for bulk GaSb and GaAs at $T=0$ K in the absence of strain. Temperature and strain effects in the GaSb barrier and GaAs substrate are included using the same rigid shift model as defined in Eq. (58). Note that the dielectric functions in GaSb and GaAs are modulated by the coherent phonon strain field as it propagates through the structure.

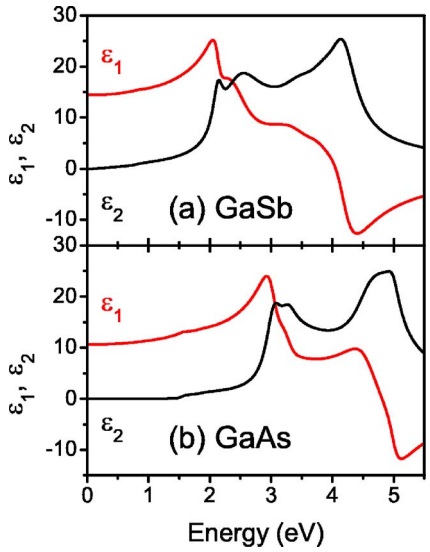

FIG. 3. (Color online) Model dielectric functions at $T=0$ K as a function of photon energy for (a) GaSb and (b) GaAs used in calculating the dielectric functions in the GaSb barrier and GaAs substrate.

IV. RESULTS AND DISCUSSION

A. Quantum well electronic states

The 25 nm thick ferromagnetic $In_{0.91}Mn_{0.09}As$ quantum well is shown schematically in Fig. 1. The quantum well is p type with a free hole density estimated to be $p \approx 10^{19}$ cm^{-3} and a Curie temperature of $T_c=55$ K. The computed band structure of the 25 nm ferromagnetic $In_{0.91}Mn_{0.09}As$ quantum well in the axial approximation, assuming infinite barriers, is shown in Fig. 4 as a function of $k_{\|}$ for temperatures above and below the Curie temperature. The Fermi energies E_f corresponding to a free hole density of $p=10^{19}$ cm^{-3} are indicated by short horizontal lines in Fig. 4. The band structure well above the Curie temperature ($T=300$ K) is shown in Fig. 4(a). Far above the Curie temperature, the average Mn spin $\langle S_z \rangle$ vanishes, the sample is nonmagnetic, and the computed subbands are doubly degenerate. Below the Curie temperature, the quantum well becomes ferromagnetic with a nonvanishing $\langle S_z \rangle$ and the doubly degenerate subbands in Fig. 4(a) become spin-split as can be seen in Fig. 4(b).

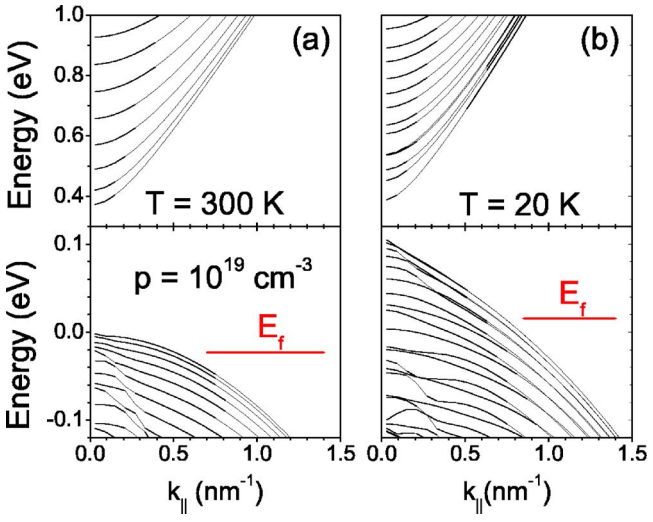

FIG. 4. (Color online) Band structure of a 25 nm ferromagnetic $In_{1-x}Mn_xAs$ quantum well with infinite barriers and $x=9\%$ at (a) $T=300$ K and (b) $T=20$ K. The Curie temperature is taken to be $T_c=55$ K. The Fermi energies E_f for a hole density of $p=10^{19}$ cm^{-3} are indicated by the horizontal lines.

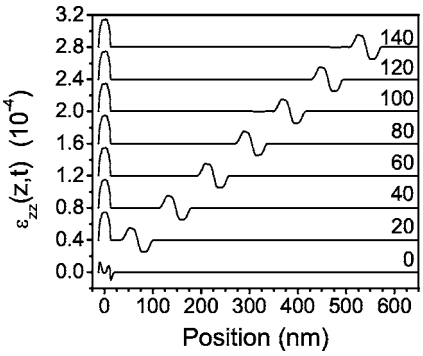

FIG. 5. Coherent phonon strain field as a function of position for delay times ranging from 0 to 140 ps. The curves have been offset for clarity.

B. Coherent phonon generation and propagation

The coherent phonon lattice displacement, $U(z,t)$, obtained from the loaded string equation (43) gives rise to strain tensor components $\varepsilon_{xx}(z,t)$, $\varepsilon_{yy}(z,t)$, and $\varepsilon_{zz}(z,t)$ as defined in Eq. (50). The coherent phonon strain tensor component $\varepsilon_{zz}(z,t)$ is shown in Fig. 5 as a function of position in the sample for several equally spaced delay times ranging from 0 to 140 ps.

Following photogeneration of carriers by the pump, a localized strain appears in the quantum well as can be seen in Fig. 5. This is due to near steady-state loading by the driving function at long times. Assuming the driving function $S(z,t)$ is approximately time independent at long times, the loaded string equation (43) can be integrated once in the steady-state limit. The resulting steady-state strain is

$$\varepsilon_{zz}(z) = \frac{\partial U(z)}{\partial z} = -\int_{-\infty}^{z} dz' \frac{S(z')}{C_s^2}, \tag{60}$$

where C_s is the longitudinal acoustic sound speed in the $In_xMn_{1-x}As$ quantum well and $S(z')$ is the approximately time-independent driving function left behind in the quantum well at long times. The fact that the steady-state strain is localized in the well follows directly from the sum rule (48).

In addition to the localized strain, a transient strain pulse propagates into the GaSb barrier at the longitudinal acoustic sound speed. Two transient strain pulses are generated in the well, one propagating to the left and the other to the right. The leftward propagating pulse is totally reflected off the semiconductor-air interface and trails the rightward propagating pulse as it propagates into the GaSb barrier.

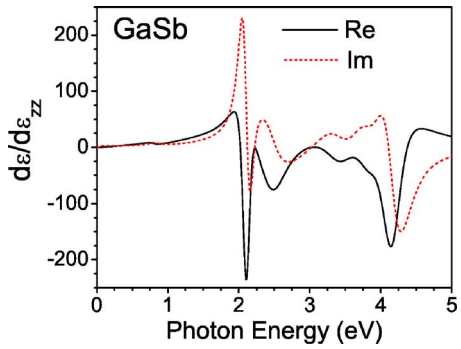

FIG. 6. (Color online) Derivative of the complex GaSb dielectric function with respect to strain as a function of the probe photon energy. The solid line is the real part and the dashed line is the imaginary part.

C. Differential reflectivity

The oscillation observed in the differential reflectivity can be attributed to propagation of the strain pulse through the structure. During most of the experiment, the traveling strain pulse is in the GaSb barrier shown schematically in Fig. 1.

The propagating strain tensor shown in Fig. 5 alters the dielectric function in the structure. The change in the complex dielectric function due to coherent phonon wave packets is given by

$$\Delta\varepsilon(\hbar\omega,z,t) = \frac{d\varepsilon(\hbar\omega,z)}{d\varepsilon_{zz}}\varepsilon_{zz}(z,t), \tag{61}$$

where the total derivative with respect to strain, $d\varepsilon(\hbar\omega,z)/d\varepsilon_{zz}$, is piecewise constant in z having different values in the $In_xMn_{1-x}As$ well, the GaSb barrier, and the GaAs substrate.

The total derivative with respect to strain in Eq. (61) is obtained from the Adachi-type model dielectric functions by differentiating Eq. (58) with respect to ε_{zz} taking care to eliminate ε_{xx} and ε_{yy} in favor of ε_{zz} using Eq. (50). In the case of GaSb, the real and imaginary parts of $d\varepsilon/d\varepsilon_{zz}$ are plotted as a function of the probe photon energy in Fig. 6. As seen in Fig. 6 the perturbation in the dielectric function per unit strain, i.e., the dielectric function strain sensitivity, is a function of the probe energy. In particular, there is a giant peak in the dielectric function strain sensitivity at the GaSb E_1 transition near 2.0 eV. Consequently, the best probe wavelength for observing coherent phonon differential reflectivity oscillations is in the region around the E_1 transition.

The differential reflectivity at a given probe delay time is obtained from the dielectric function by solving Maxwell's equations in the entire structure using the transfer matrix formalism as described earlier. If we use the complete time- and space-dependent dielectric function defined in Eq. (59) including the quantum well, Drude, and background contributions, we can compute the total differential reflectivity containing the coherent phonon oscillation and transient carrier relaxation effects.

Our theoretical results are compared with the experiment in Fig. 7 where we plot the experimental and theoretical differential reflectivity spectra for probe wavelengths of 650 and 775 nm. In both cases there is an initial sharp drop in the differential reflectivity which we attribute to free carrier Drude absorption by the hot carriers created by the pump.

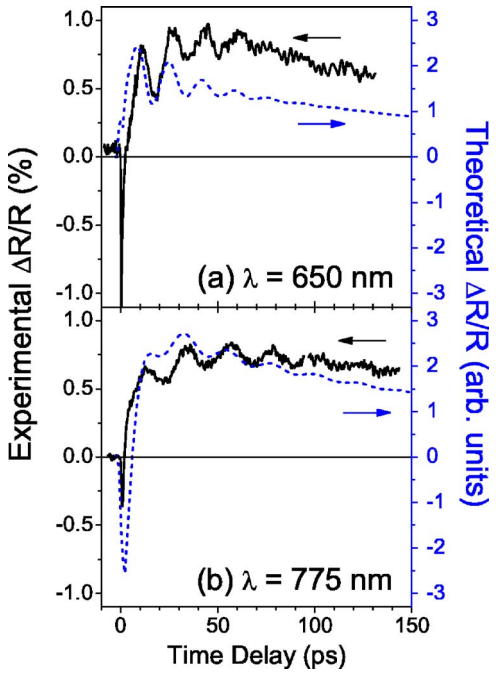

FIG. 7. (Color online) Theoretical and experimental differential reflectivity for probe wavelengths of (a) 650 and (b) 775 nm due to variations in the time- and space-dependent dielectric functions.

The photogenerated hot carriers relax back to quasiequilibrium distributions at their respective band edges through emission of confined LO phonons. The relaxation of photogenerated carriers by LO phonons alters the quantum well dielectric function in Eq. (55) through changes in the time-dependent distribution functions. This carrier cooling by LO phonon emission results in the subsequent rise in the differential reflectivity traces seen in Fig. 7.

In addition to carrier cooling by LO phonon emission, electron-hole pairs recombine through trapping at midgap defects with $\tau_0 \approx 200$ ps. This gives rise to the slow decay in the differential reflectivity at long times seen in Fig. 7. At short times, electron-hole pair recombination is enhanced since the Shockley-Read recombination time $\tau(t)$ is a monotonically decreasing function of the photogenerated electron-hole pair density.

For delay times of less than 20 ps, our theory does not agree very well with the experiment. For delay times greater than 20 ps, however, the theory reproduces the experimental results surprisingly well. In particular, the period and amplitude of the reflectivity oscillations in relation to the height of the plateau as well as the decay of the reflectivity oscillations with delay time are in good agreement with experiment.

The oscillations in differential reflectivity seen in Fig. 7 are due to changes in the background dielectric function induced by the propagating coherent strain pulse seen in Fig. 5. If we compute the probe differential reflectivity neglecting the quantum well and Drude contributions to the total dielectric function in Eq. (59) and retain only the background contribution, we get the coherent acoustic phonon differential

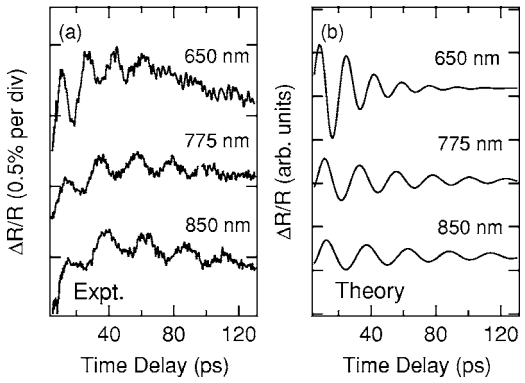

FIG. 8. Experimental (a) and theoretical (b) coherent phonon differential reflectivity oscillations for probe wavelengths of 650, 775, and 850 nm.

reflectivity oscillation absent the transient relaxation signal.

In Fig. 8 the computed coherent phonon differential reflectivity oscillations are shown as a function of time delay for probe wavelengths of 650, 775, and 850 nm, corresponding to photon energies of 1.9, 1.6, and 1.46 eV, respectively. The theoretical differential reflectivity curves in Fig. 8(b) agree well with the experimentally measured differential reflectivity seen in Fig. 8(a) after subtraction of the transient background signal. As we go from 650 to 850 nm, the differential reflectivity oscillation period becomes longer.

The reflectivity oscillations can be qualitatively understood as follows. The propagating strain pulse in Fig. 5 gives rise to a perturbation in the GaSb dielectric function which propagates at the acoustic sound speed. The sample thus acts as a Fabry-Perot interferometer and a simple geometrical optics argument shows that the period for the reflectivity oscillations due to the propagating coherent acoustic phonon wave packet is approximately[12]

$$T = \frac{\lambda}{2C_s n(\lambda)}, \tag{62}$$

where $\lambda = 2\pi c/\omega$ is the probe wavelength, C_s is the LA sound speed in the GaSb barrier, and $n(\lambda)$ is the wavelength-dependent refractive index. The refractive index can be obtained from the GaSb model dielectric function in Fig. 3(a) as[50]

$$n(\lambda) = \sqrt{\tfrac{1}{2}[\varepsilon_1(\lambda) + \sqrt{\varepsilon_1(\lambda)^2 + \varepsilon_2(\lambda)^2}]}. \tag{63}$$

In Fig. 9 we have plotted experimentally measured coherent phonon differential reflectivity oscillation periods as a function of probe wavelength as solid circles. The solid line shows the oscillation period vs probe wavelength estimated using Eq. (62). The excellent agreement between theory and experiment is compelling evidence that the reflectivity oscillations seen in the experiments are induced by propagating coherent acoustic phonons in the GaSb barrier.

In going from a probe wavelength of 650 to 850 nm in Fig. 8, we note that the initial amplitude of the differential reflectivity oscillation decreases with increasing probe wavelength. At the same time these oscillations become more weakly damped. The reason for the reduction in amplitude of

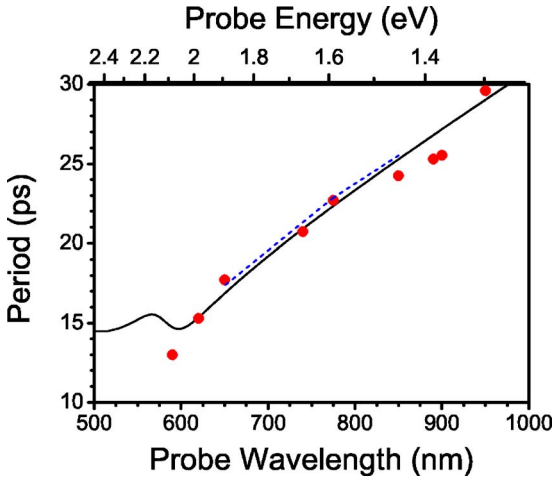

FIG. 9. (Color online) Coherent phonon differential reflectivity oscillation period vs probe wavelength. The experimental data are shown as solid circles, the dashed line shows the oscillation period calculated from the theory described in the text, and the solid line shows the oscillation period estimated from Eq. (62).

the oscillations can be found in Fig. 10 where we plot $d\varepsilon/d\varepsilon_{zz}$ as a function of probe wavelength. As the probe wavelength increases (and the photon energy decreases), the strength of the perturbation of the dielectric function due to the propagating coherent phonon strain defined in Eq. (61) decreases. This accounts for the observed reduction in the initial amplitude of the differential reflectivity oscillations as we go to higher wavelengths. The increased damping of the differential reflectivity oscillations with decreasing probe wavelength is simply due to the fact that the absorption coefficient in GaSb is rapidly decreasing with wavelength in this wavelength range as can be inferred from the imaginary part of the GaSb dielectric function plotted in Fig. 3(a).

V. CONCLUSIONS

In summary, we have performed calculations and modeled time-dependent two-color differential reflectivity experi-

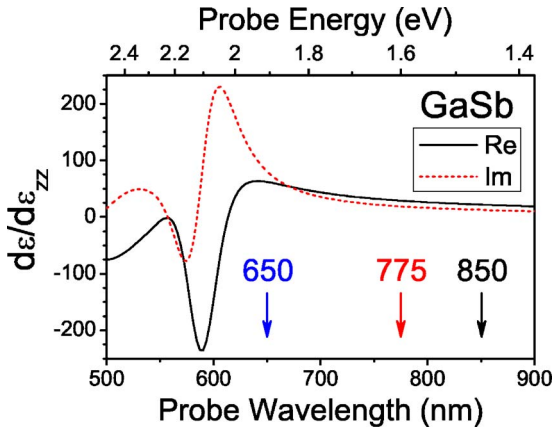

FIG. 10. (Color online) Derivative of the complex GaSb dielectric function with respect to strain as a function of the probe wavelength in the experimentally relevant wavelength range. The solid line is the real part and the dashed line is the imaginary part.

ments on a ferromagnetic $In_xMn_{1-x}As/GaSb$ heterostructure. We have observed large amplitude reflectivity oscillations resulting from the generation of coherent acoustic phonon wave packets in the $In_xMn_{1-x}As$ quantum well and their subsequent propagation into the GaSb layer. The propagation of these coherent, localized strain pulses into the GaSb buffer results in a position- and frequency-dependent dielectric function.

To take into account the time-dependent background differential reflectivity, we modeled the two color pump-probe reflectivity experiments in a Boltzmann equation formalism. Electronic structure was calculated using $\vec{k}\cdot\vec{p}$ theory in a confined $In_xMn_{1-x}As$ layer. We included (1) photogeneration of hot carriers in the $In_xMn_{1-x}As$ quantum well by a pump laser and (2) their subsequent cooling by emission of confined LO phonons. Recombination of electron-hole pairs via the Schockley-Read carrier trapping mechanism was also included in a simple relaxation time approximation.

Our results agree remarkably well with the experimental coherent phonon oscillations and reasonably well with the time-dependent background signal and capture the major qualitative trends of the data. We identify three key effects which contribute to the backgrounds signal: (1) the enhanced Drude absorption resulting from the increase in carriers from the laser photoexcitation [negative $\Delta R/R$], (2) the relaxation dynamics associated with the decay of the highly nonequilibrium photoexcited carrier distribution [positive $\Delta R/R$], and (3) the trapping and the nonradiative recombination of the photoexcited carriers resulting from the high density of defects in the $In_xMn_{1-x}As$ layer (positive $\Delta R/R$).

ACKNOWLEDGMENTS

This work was supported by DOE through Grant No. DE-FG02–02ER45984, and by NSF through Grant Nos. DMR-0134058 (CAREER), DMR-0325474 (ITR), and INT-0221704.

[1] I. Žutić, J. Fabian, and S. Das Sarma, Rev. Mod. Phys. **76**, 323 (2004).
[2] H. Ohno, Science **281**, 951 (1998).
[3] H. Ohno, Science **291**, 840 (2001).
[4] M. A. Zudov, J. Kono, Y. H. Matsuda, T. Ikaida, N. Miura, H. Munekata, G. D. Sanders, Y. Sun, and C. J. Stanton, Phys. Rev. B **66**, 161307(R) (2002).
[5] G. D. Sanders, Y. Sun, F. V. Kyrychenko, C. J. Stanton, G. A. Khodaparast, M. A. Zudov, J. Kono, Y. H. Matsuda, N. Miura, and H. Munekata, Phys. Rev. B **68**, 165205 (2003).
[6] G. D. Sanders, Y. Sun, C. J. Stanton, G. A. Khodaparast, J. Kono, Y. H. Matsuda, N. Miura, T. Slupinski, A. Oiwa, and H. Munekata, J. Appl. Phys. **93**, 6897 (2003).
[7] G. D. Sanders, Y. Sun, C. J. Stanton, G. A. Khodaparast, J. Kono, D. S. King, Y. H. Matsuda, S. Ikeda, N. Miura, and A. Oiwa, Physica E (Amsterdam) **20**, 378 (2004).
[8] Y. H. Matsuda, G. A. Khodaparast, M. A. Zudov, J. Kono, Y. Sun, F. V. Kyrychenko, G. D. Sanders, N. Miura, S. Ikeda, and Y. Hashimoto, Phys. Rev. B **70**, 195211 (2004).
[9] A. V. Kuznetsov and C. J. Stanton, Phys. Rev. B **51**, 7555 (1995).
[10] T. Dekorsy, T. Pfeifer, W. Kutt, and H. Kurz, Phys. Rev. B **47**, 3842 (1993).
[11] G.-W. Chern, C.-K. Sun, G. D. Sanders, and C. J. Stanton, in *Topics in Applied Physics*, edited by K.-T. Tsen (Springer-Verlag, New York, 2004), Vol. 92, pp. 339–394.
[12] J. S. Yahng, Y. D. Jho, K. J. Yee, E. Oh, J. C. Woo, D. S. Kim, G. D. Sanders, and C. J. Stanton, Appl. Phys. Lett. **80**, 4723 (2002).
[13] C. J. Stanton, G. D. Sanders, R. Liu, G.-W. Chern, C.-K. Sun, J. S. Yahng, Y. D. Jho, J. Y. Sohn, E. Oh, and D. S. Kim, Superlattices Microstruct. **34**, 525 (2003).
[14] R. Liu, C. S. Kim, G. D. Sanders, C. J. Stanton, J. S. Yahng, Y. D. Jho, K. J. Yee, E. Oh, and D. S. Kim, Phys. Rev. B **72**, 195335 (2005).
[15] J. Wang, Y. Hashimoto, J. Kono, A. Oiwa, H. Munekata, G. D. Sanders, and C. J. Stanton, Phys. Rev. B **72**, 153311 (2005).
[16] J. Wang, J. Kono, A. Oiwa, H. Munekata, and C. J. Stanton, Superlattices Microstruct. **34**, 563 (2003).
[17] T. Slupinski, A. Oiwa, S. Yanagi, and H. Munekata, J. Cryst. Growth **237-239**, 1326 (2002).
[18] J. Wang, G. A. Khodaparast, J. Kono, A. Oiwa, and H. Munekata, J. Mod. Opt. **51**, 2771 (2004).
[19] C. K. Pidgeon and R. N. Brown, Phys. Rev. **146**, 575 (1966).
[20] A. L. Efros and M. Rosen, Phys. Rev. B **58**, 7120 (1988).
[21] S. C. Jain, J. M. McGregor, and D. J. Roulston, J. Appl. Phys. **68**, 3747 (1990).
[22] Y. P. Varshni, Physica (Amsterdam) **34**, 149 (1967).
[23] I. Vurgaftman, J. R. Meyer, and L. R. Ram-Mohan, J. Appl. Phys. **89**, 5815 (2001).
[24] A. Baldereschi and N. O. Lipari, Phys. Rev. B **8**, 2697 (1973).
[25] J. M. Luttinger, Phys. Rev. **102**, 1030 (1956).
[26] J. Kossut, Semicond. Semimetals **25**, 183 (1988).
[27] J. K. Furdyna, J. Appl. Phys. **64**, R29 (1988).
[28] H. Munekata, H. Ohno, S. von Molnár, A. Segmüller, L. L. Chang, and L. Esaki, Phys. Rev. Lett. **63**, 1849 (1989).
[29] H. Munekata, H. Ohno, S. von Molnár, A. Harwitt, A. Segmüller, and L. L. Chang, J. Vac. Sci. Technol. B **8**, 176 (1990).
[30] H. Ohno, H. Munekata, S. von Molnár, and L. L. Chang, J. Appl. Phys. **69**, 6103 (1991).
[31] S. von Molnár, H. Munekata, H. Ohno, and L. L. Chang, J. Magn. Magn. Mater. **93**, 356 (1991).
[32] G. D. Sanders and C. J. Stanton, Phys. Rev. B **57**, 9148 (1998).
[33] W. H. Press, S. A. Teukolsky, W. T. Vetterling, and B. P. Flannery, *Numerical Recipes* (Cambridge University Press, New York, 1992).
[34] J. S. Blakemore, *Semiconductor Statistics* (Dover, New York, 1987).
[35] R. Fuchs and K. L. Kleiwer, Phys. Rev. **140**, 2076 (1965).
[36] G. D. Sanders, C. J. Stanton, and C. S. Kim, Phys. Rev. B **64**, 235316 (2001).
[37] G. D. Sanders, C. J. Stanton, and C. S. Kim, Phys. Rev. B **66**, 079903(E) (2002).

[38] N. V. Chigarev, D. Y. Paraschuk, X. Y. Pan, and V. E. Gusev, Phys. Rev. B **61**, 15837 (2000).
[39] S. L. Chuang, *Physics of Optoelectronic Devices* (Wiley, New York, 1995).
[40] W. Schäfer and M. Wegener, *Semiconductor Optics and Transport Phenomena* (Springer, New York, 2002).
[41] F. Bassani and G. P. Parravicini, *Electronic States and Optical Transitions in Solids* (Pergamon, New York, 1975).
[42] S. Adachi, J. Appl. Phys. **66**, 6030 (1989).
[43] A. B. Djurišić, A. D. Radić, P. C. K. Kwok, E. H. Li, and M. L. Majewski, J. Appl. Phys. **85**, 3638 (1999).
[44] C. Thomsen, J. Strait, Z. Vardeny, H. J. Maris, J. Tauc, and J. J. Hauser, Phys. Rev. Lett. **53**, 989 (1984).
[45] C. Thomsen, H. T. Grahn, H. J. Maris, and J. Tauc, Phys. Rev. B **34**, 4129 (1986).
[46] D. Rönnow, N. E. Christensen, and M. Cardona, Phys. Rev. B **59**, 5575 (1999).
[47] M. Munoz, K. Wei, F. H. Pollak, J. L. Freeouf, and G. W. Charache, Phys. Rev. B **60**, 8105 (1999).
[48] A. B. Djurišić, Y. Chan, and E. H. Li, Semicond. Sci. Technol. **16**, 902 (2001).
[49] A. D. Rakić and M. L. Majewski, J. Appl. Phys. **80**, 5909 (1996).
[50] H. Haug and S. W. Koch, *Quantum Theory of the Optical and Electronic Properties of Semiconductors* (World Scientific, New Jersey, 1993).